Superconductivity of $MoBe_{22}$ and WBe_{22} at ambient- and under applied-pressure conditions

T. Shiroka,[1,2,*] T. Shang,[3,†] M. Juckel,[4] M. Krnel,[4] M. König,[4] U. Burkhardt,[4] P. Koželj,[4,‡] R. Gupta,[1] Yu. Prots,[4] and E. Svanidze[4,§]

[1]*Laboratory for Muon-Spin Spectroscopy, Paul Scherrer Institut, Villigen PSI, Switzerland*
[2]*Laboratorium für Festkörperphysik, ETH Zürich, CH-8093 Zürich, Switzerland*
[3]*Key Laboratory of Polar Materials and Devices (MOE), School of Physics and Electronic Science, East China Normal University, Shanghai 200241, China*
[4]*Max Planck Institute for Chemical Physics of Solids, D-01187 Dresden, Germany*

(Received 15 February 2022; accepted 31 May 2022; published 27 June 2022)

$MoBe_{22}$ and WBe_{22} compounds belong to the binary XBe_{22} ($X = 4d$ or $5d$ metal) family of superconductors, whose critical temperature depends strongly on X. Despite the multiphase nature of these samples, it is possible to investigate the superconducting properties of $MoBe_{22}$ and WBe_{22} at the macro- and microscopic level. A concurrent analysis by means of magnetization and heat-capacity measurements, as well as muon-spin spectroscopy (μSR) was implemented. At ambient pressure, both compounds enter the superconducting state below 2.6 ± 0.1 K ($MoBe_{22}$) and 4.1 ± 0.10 K (WBe_{22}) and show modest upper critical fields [$(\mu_0 H_{c2}(0) = 48 \pm 1$ mT and $\mu_0 H_{c2}(0) = 58 \pm 1$ mT, respectively]. In WBe_{22}, the temperature-dependent superfluid density suggests a fully gapped superconducting state, well-described by an s-wave model with a single energy gap. Heat-capacity data confirm that such a model applies to both compounds. Finally, *ac* magnetic susceptibility measurements under applied pressures up to 2.1 GPa reveal a linear suppression of the superconducting temperature, typical of conventional superconducting compounds.

DOI: 10.1103/PhysRevMaterials.6.064804

I. INTRODUCTION

As one of the lightest elements, beryllium exhibits lattice vibrations of high frequency, a necessary condition for achieving superconductivity with a sizable critical temperature. Nevertheless, the critical temperature of elemental beryllium is only 0.026 K [1]. The value of T_c is also affected by the electron-phonon coupling strength (typically large in elements with covalent-bonding tendencies) and the density of states at the Fermi level $N(E_F)$ (rather low in elemental Be). In particular, $N(E_F)$ depends on the details of crystal structure and atomic volume—two factors which are best illustrated by metal-hydride superconductors under pressure [2]. Here, recent work has demonstrated that, in actinium hydrides at 200 GPa, purely phonon-mediated superconductivity with T_c up to 250 K [3] is likely to occur because these materials contain metal atoms that are close to populating a new electronic subshell—for example, d^1 (Sc, Y, La, and Ac) or p^0 (Be, Mg, and Ca). In this case, the electronic structure becomes highly sensitive to the positions of the neighboring atoms, resulting in stronger electron-phonon interactions and higher $N(E_F)$. Based on this, Be-rich alloys may achieve a T_c much higher than that of elemental Be, a prediction which is correct for $ReBe_{22}$ ($T_c \sim 9.6$ K [4,5]). A detailed examination of $ReBe_{22}$ revealed it to be a multigap type-II superconductor, well-described by an isotropic s-wave model. Here, the enhanced T_c (compared to elemental Be) seems to arise from a *concomitant* increase of both electron-phonon coupling strength and $N(E_F)$ [5]. By investigating the effects of hydrostatic pressure on $ReBe_{22}$, a 0.5 K decrease of T_c with a pressure of 1 GPa was established. Further increase in pressure does not change T_c, as confirmed by electrical resistivity measurements at even higher pressures—up to 30 GPa [6]. Another possibility to control the superconducting properties of the XBe_{22} class is to employ the isotope effect and/or the chemical pressure, whose effects are significant in this class of compounds [4]. It is, therefore, of interest to examine the isostructural $MoBe_{22}$ and WBe_{22} compounds (with their structure shown in Fig. 1), both under pressure as well as at ambient conditions.

Superconductivity of $MoBe_{22}$ and WBe_{22} has been previously reported to occur below $T_c = 2.52$ K and $T_c = 4.14$ K, respectively [4,7,8]. However, given the difficulties in synthesizing and characterizing beryllium-containing materials [9–15], neither system has been investigated thoroughly. Additionally, it has been shown that a combined analysis of specific-heat and μSR data in similar superconducting materials is highly relevant [9,16–18].

Motivated by this, we present an in-depth study of $MoBe_{22}$ and WBe_{22} by means of magnetization, *ac*-susceptibility, heat-capacity, and muon-spin spectroscopy (μSR) measure-

*Corresponding author: tshiroka@phys.ethz.ch
†Corresponding author: tshang@phy.ecnu.edu.cn
‡Present address: Jožef Stefan Institute and Faculty of Mathematics and Physics, University of Ljubljana, SI-1000 Ljubljana, Slovenia.
§Corresponding author: svanidze@cpfs.mpg.de

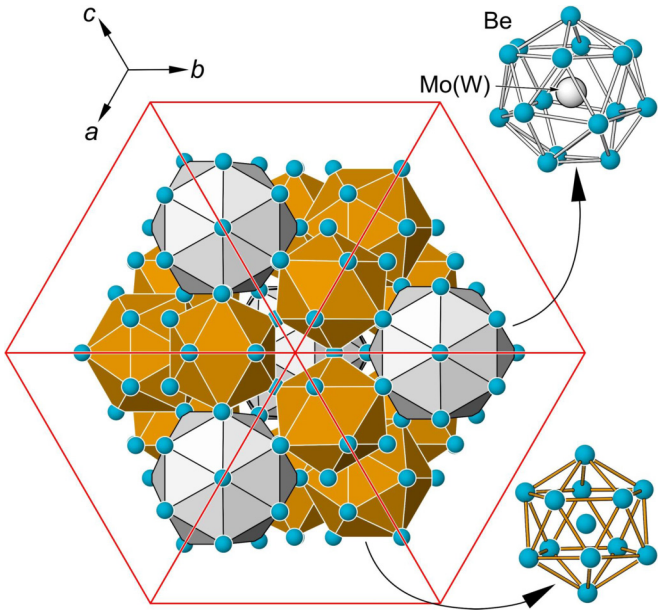

FIG. 1. The arrangement of the coordination polyhedra around Mo(W) and Be2 atoms (16*d* site) in the structures of $MoBe_{22}$ and WBe_{22}. For simplicity, only part of the unit cell is shown.

ments. In addition, we examine the effects of pressure on the superconductivity of both materials. Despite the multiphase nature of the samples, we could establish that both compounds are conventional, fully-gapped type-II superconductors, with a modest electronic specific-heat coefficient, suggestive of a negligible electron-mass enhancement. The low values of the upper critical field and the linear decrease of T_c with pressure are typical of this class of superconductors.

II. EXPERIMENTAL DETAILS

All sample preparation and handling was performed in a specialized laboratory, equipped with an argon-filled glove box system [MBraun, $p(H_2O/O_2)$ <0.1 ppm] [19]. The polycrystalline samples were synthesized by arc melting of Be (Heraeus, >99.9 wt%) with Mo or W (Chempur, 99.99%) in the 99:1 ratio. Since the amount of Be is hard to quantify analytically and given that evaporation losses of Be are unavoidable, the only way to keep the sample composition under control is by following a careful weighing protocol [12–14]. None of the samples exhibit any marked air- or moisture sensitivity. Both $MoBe_{22}$ and WBe_{22} phases melt incongruently and have a high melting temperature (1300 °C and 1520 °C, respectively [20,21]). To date, this has prevented the synthesis of single-phase XBe_{22} materials, let alone of their single crystals. In the current paper, we could successfully synthesize and characterize multiphase polycrystalline samples of both $MoBe_{22}$ and WBe_{22}, albeit with small amounts of foreign phases (see below).

Given the high mechanical hardness and ductility of both samples, it was not possible to perform reliable powder diffraction experiments. Instead, a metallographic analysis of the polished sample surfaces was performed *via* energy-dispersive x-ray spectroscopy on a Jeol JSM 6610 scanning electron microscope, equipped with an UltraDry EDS detector (ThermoFisher NSS7). The microstructures of the Mo-Be and W-Be samples show very similar arrangement of the phases. In both cases, the material-contrast images recorded with a backscattered electron detector show bright dendrites embedded in a matrix. The matrix is formed by a mixture of dark grey fibers within a dark, almost globular phase [see Figs. 2(a), 2(b), 3(a), and 3(b) for Mo-Be and W-Be, respectively]. The high transition-metal concentration of the bright dendritic and the fiber-shaped phases, as indicated by their brightness in the BSE images, is confirmed by the qualitative comparison of the EDX spectra. The local EDX spectra are extracted from equal areas of the EDX mapping data and show decreasing intensities of the transition-metal x-ray lines, e.g., Mo *L* line for the Mo-Be samples and W *L* and *M* lines for the W-Be samples for the darker phases. SEM analyses were performed with acceleration voltages of 10 kV or 20 kV for the Mo-Be and W-Be samples, respectively. $MoBe_{22}$ and WBe_{22} can be assigned to the dark phase of the respective microstructure due to the significant intensities of the transition-metal x-ray lines. Additionally, solid Be does not show any significant solubility in Mo or W. Based on the published binary phase diagrams of Mo-Be and W-Be [20,21], it is reasonable to assume that the congruent melting phases $MoBe_2$ and WBe_2 form the respective dendritic phase, while $MoBe_{12}$ and WBe_{12} form the fiber-shaped phases with an intermediate transition-metal concentration. We have also established that the impurity phases Mo/WBe_2 and Mo/WBe_{12} do not show any magnetic transition down to $T = 1.8$ K. Based on Figs. 2 and 3, we estimate that the samples from the current study contain ∼40% of the Mo/WBe_{22}, ∼30% of the Mo/WBe_{12}, and ∼30% of the Mo/WBe_2 phases.

Since the previously reported structures of $MoBe_{22}$ and WBe_{22} were obtained from powder diffraction data [22,23], we performed single-crystal x-ray diffraction measurements. For this, a single-phase cuboid, consisting predominantly of either WBe_{22} or $MoBe_{22}$ material, was fabricated in a multistep process using a Xe-plasma focused-ion-beam (FEI Helios G4 PFIB). With a size of $\sim 30 \times 30 \times 30\ \mu m^3$, it was ideally suited for single-crystal diffraction experiments [see Figs. 2(c) and 3(c)]. The relevant diffraction data were collected using a Rigaku AFC7 diffractometer, equipped with a Saturn 724+ CCD detector and Mo Kα radiation source ($\lambda = 0.71073$ Å). SHELXL software was used for the structural refinement. The results of the crystallographic characterization of $MoBe_{22}$ and WBe_{22} are provided in Tables S1 and S2, respectively [24].

The magnetic properties of both compounds were studied using a Quantum Design (QD) Magnetic Property Measurement System in the temperature range from 1.8 K to 300 K, in applied magnetic fields up to 7 T. The specific-heat data were collected on a QD Physical Property Measurement System in the temperature range from 0.4 K to 10 K, in magnetic fields up to 9 T. Both magnetization and specific-heat measurements were performed on bulk samples, showing minimal variation of superconducting features between the different sample batches or pieces. Given the multiphase nature of our samples, it was not possible to carry out reliable electrical resistivity measurements.

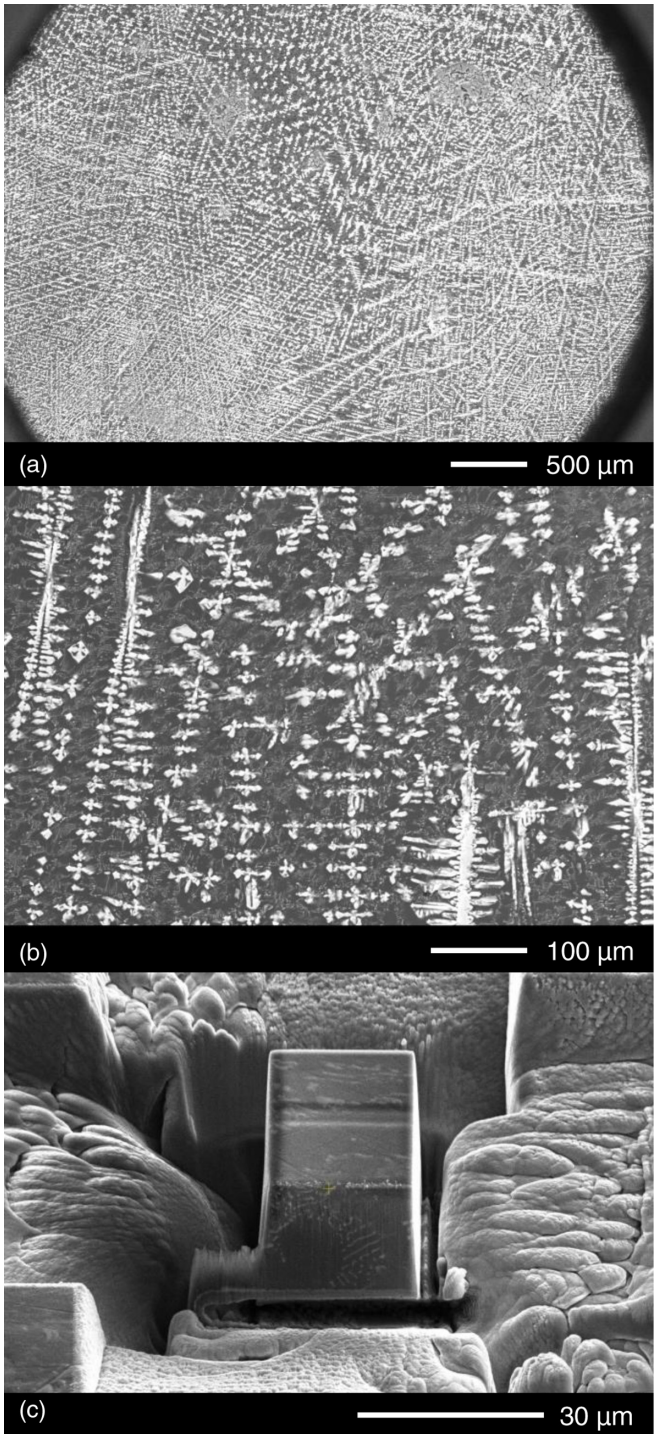

FIG. 2. (a), (b) Backscatter electron micrographs of $MoBe_{22}$ sample surface at various magnifications. (c) A cuboid of $MoBe_{22}$, used for the single-crystal diffraction experiments, prepared using focused-ion beam.

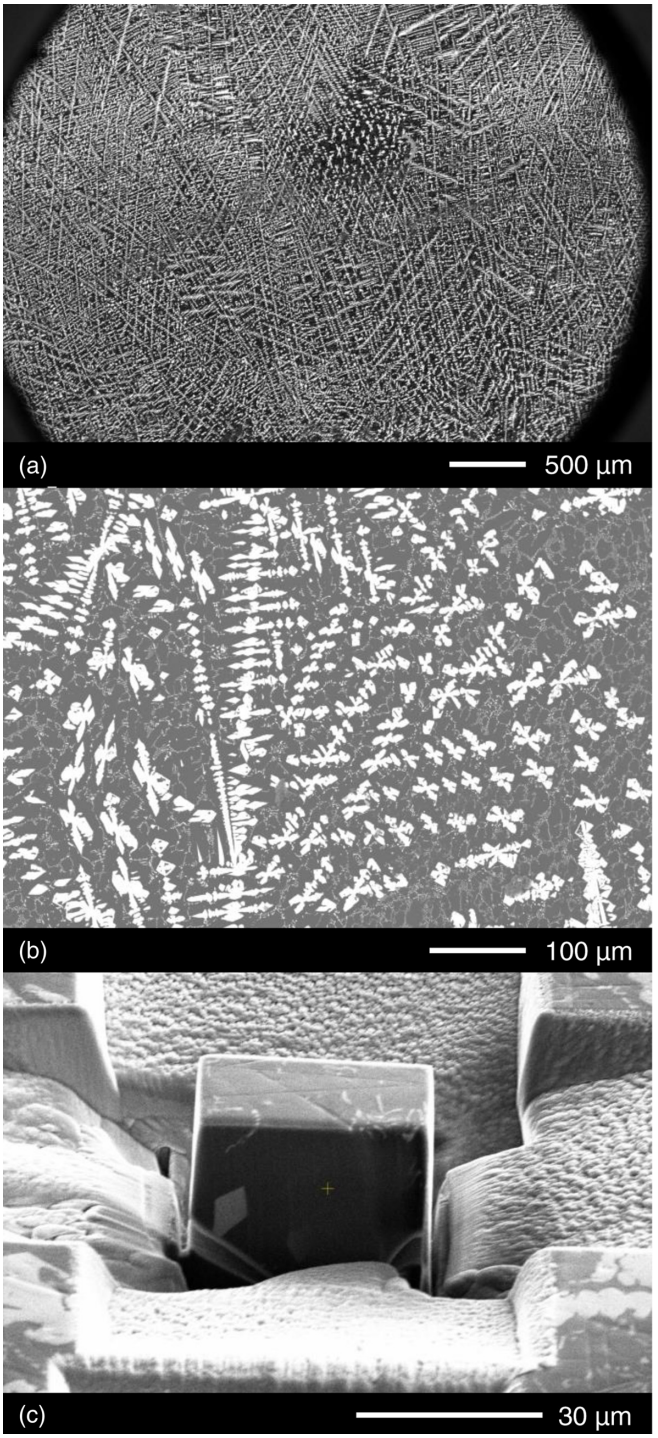

FIG. 3. (a), (b) Backscatter electron micrographs of WBe_{22} sample surface at various magnifications. (c) A cuboid of WBe_{22}, used for the single-crystal diffraction experiments, prepared using focused-ion beam.

The muon-spin spectroscopy measurements were performed at the Dolly (zero pressure) and GPD (under pressure) spectrometers of the Swiss muon source at Paul Scherrer Institut, Villigen, Switzerland. The μSR data were analyzed by means of the MUSRFIT software package [25]. In the zero-pressure case, three discs of ca. 8 mm in diameter were positioned so as to cover more than 85% of the muon-beam cross section, thus resulting in low-background high-quality μSR signals. The applied field of 15 mT yielded a T_c of 3.5 K for WBe_{22}, significantly lower than $T_c(0) = 4.09$ K, hinting at a rather low H_{c2} value—see below. The same sample was successively used to fill a dual-walled WC pressure cell

(channel diameter 6 mm) up to a height of 12 mm. The dual-wall configuration allows the cell to reach pressures of up to 2.3 GPa, albeit at the expense of a relatively low sample-to-cell μSR signal ratio. We used Daphne 7373 oil as a pressure transmitting medium, whose properties under a broad range of p–T conditions are well-known [26,27].

ac susceptibility measurements under pressure were performed using the same pressure cell used for the μSR measurements [28,29]. In our case, the excitation and pick-up coils were wound outside the cell. While this setup generally has a low sensitivity, it is sufficient for successfully detecting the superconducting transition [30]. An Ametek 7270 DSP lock-in amplifier was used to capture the 72-Hz *ac* signal, successively measured by a Keithley 2000 digital multimeter.

III. RESULTS AND DISCUSSION

A. Crystal structure description

In previous studies [22,23], the structure of $MoBe_{22}$ and WBe_{22} was established by comparing the experimental powder diffraction patterns (photographic data) with calculated patterns, obtained on the basis of the $Mg_3Cr_2Al_{18}$ [31] structure (E phase). The atomic coordinates were taken from the latter model and, therefore, were not refined. For this reason, a reinvestigation of the crystal structure of $MoBe_{22}$ and WBe_{22} was performed to obtain a more precise crystallographic description.

Both structures are isotypic with $ZrZn_{22}$ [32]. The substitution variants were also described for $CeCr_2Al_{20}$ [33] and $Mg_3Cr_2Al_{18}$ [31]. The crystal structure of $MoBe_{22}$ (WBe_{22}) can be represented as an arrangement of Frank-Kasper polyhedra with 16 and 12 apexes (icosahedra) formed by Be species around the Mo and Be2 positions, respectively. The polyhedra are only connected to each other through their vertices. Each [$MoBe_{16}$] polyhedron has in its neighborhood four identical groups in tetrahedral arrangement and 12 [$BeBe_{12}$] icosahedra (see Fig. 1). The described polyhedra resemble the atomic coordination of Mg and Cu, respectively, in the Laves phase $MgCu_2$ [34].

B. Magnetization and specific heat

The superconductivity of $MoBe_{22}$ and WBe_{22} was previously reported to occur below $T_c = 2.52$ K and 4.14 K [4,7,8], respectively. In both materials, the first indication of superconductivity is given by a sharp diamagnetic transition at the respective T_c value, as shown in Figs. 4(a) and 4(b) [35]. For $\mu_0 H > 2$ mT ($MoBe_{22}$) and $\mu_0 H > 10$ mT (WBe_{22}), the low-temperature plateau is not visible, due to it being below the minimum accessible temperature of 1.8 K. Normally, the lower critical field value H_{c1} is defined as the field at which the $M(H)$ curve deviates from the line having the initial slope of $M(H)$. However, in our case, the lowest experimentally accessible temperature was not sufficient to allow for such an analysis. In addition, in the $MoBe_{22}$ sample, the origin of the kink around 2.4 K is not yet clear. Nonetheless, since the shielding fraction is above 100% and none of the identified impurities are known to be superconductors, the superconductivity of both $MoBe_{22}$ and WBe_{22} is intrinsic.

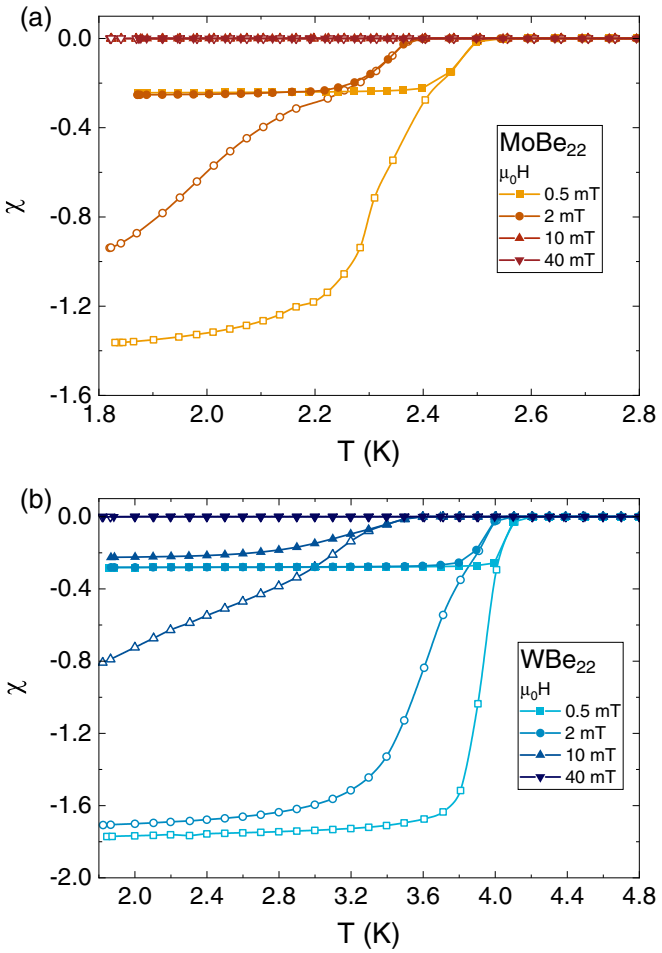

FIG. 4. Zero-field-cooled (open symbols) and field-cooled (full symbols) temperature-dependent magnetic susceptibility data for $MoBe_{22}$ (a) and WBe_{22} (b) in an applied field $0.5 \leqslant \mu_0 H \leqslant 40$ mT.

The specific-heat data of $MoBe_{22}$ and WBe_{22}, shown in Fig. 5, also confirm their bulk superconductivity. In the absence of a magnetic field, an anomaly associated with the onset of the superconducting transition is observed at $T_c = 2.55$ K and $T_c = 4.09$ K in $MoBe_{22}$ and WBe_{22}, respectively. A linear fit to C_p/T versus T^2 data [insets of Figs. 5(b) and 5(d)] provides an upper-bound estimate for the values of the Sommerfeld coefficient $\gamma_n = 6.8 \pm 0.2$ mJ $\text{mol}_{\text{f.u.}}^{-1}$ K^{-2} and $\gamma_n = 10.0 \pm 0.2$ mJ $\text{mol}_{\text{f.u.}}^{-1}$ K^{-2} for $MoBe_{22}$ and WBe_{22}, respectively. The residual electronic specific-heat coefficient $\gamma_{\text{res}} = C_e/T$ ($T = 0.35$ K, $\mu_0 H = 0$) ≈ 4 mJ $\text{mol}_{\text{f.u.}}^{-1}$ K^{-2} for both $MoBe_{22}$ and WBe_{22} samples is consistent with the presence of the secondary phases identified in Figs. 2 and 3. The multiphase nature of the samples is also likely responsible for the large difference in the β coefficients: $\beta = 0.21 \pm 0.05$ mJ $\text{mol}_{\text{f.u.}}^{-1}$ K^{-4} ($MoBe_{22}$) and $\beta = 0.05 \pm 0.01$ mJ $\text{mol}_{\text{f.u.}}^{-1}$ K^{-4} (WBe_{22}). These β values can, nevertheless, be used for a preliminary estimate of the Debye temperature (600 K $\leqslant \theta_D \leqslant$ 900 K), as well as of the electron-phonon coupling strength ($\lambda_{\text{e-ph}} \sim 0.4$). The latter value classifies both $MoBe_{22}$ and WBe_{22} as weakly-coupled superconductors.

Further evidence of conventional superconductivity in $MoBe_{22}$ and WBe_{22} is given by the value of the jump in

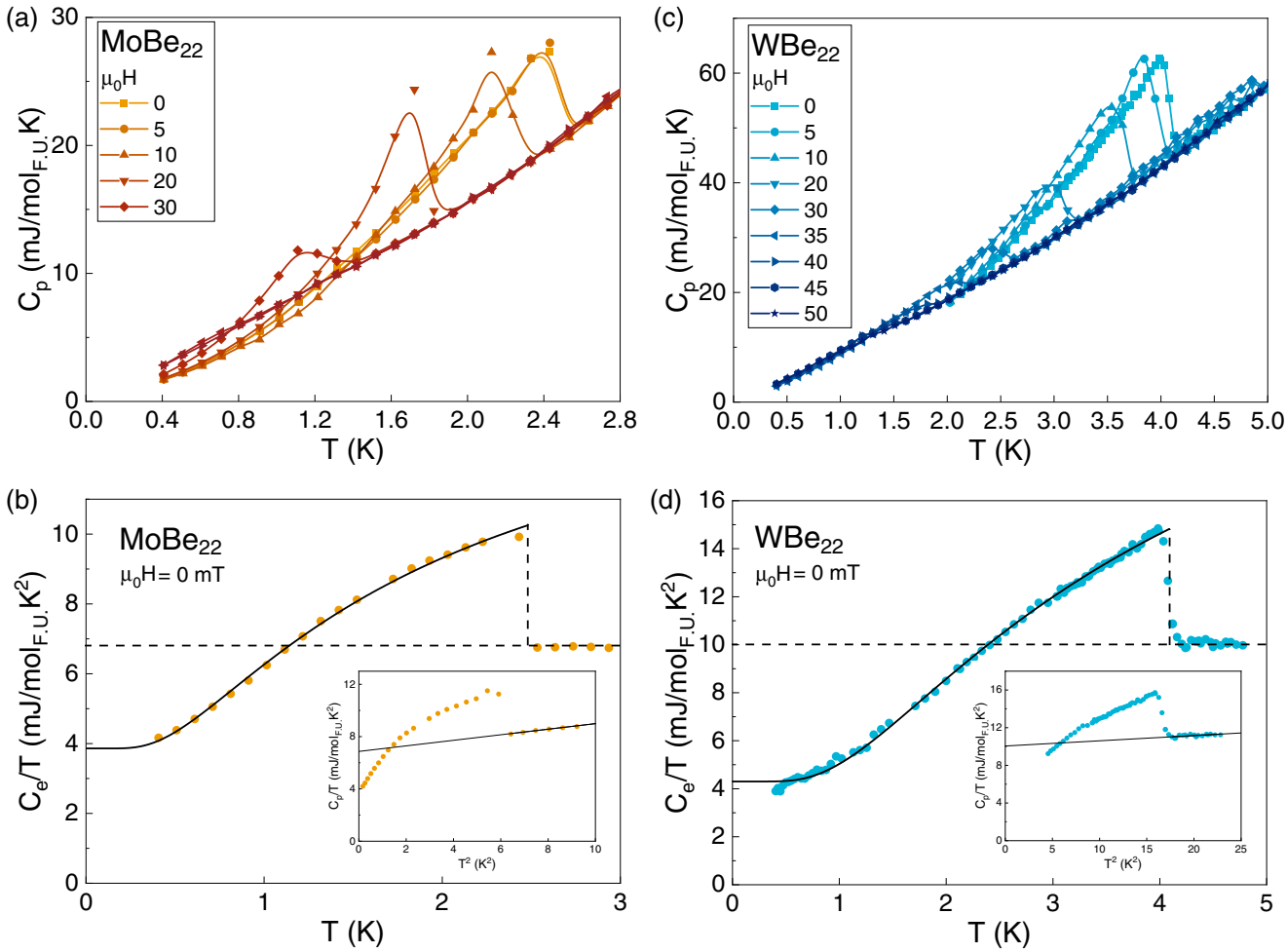

FIG. 5. Total specific heat of $MoBe_{22}$ (a) and WBe_{22} (c) as a function of temperature in an applied field $0 \leqslant \mu_0 H \leqslant 50$ mT. The electronic specific heat of $MoBe_{22}$ (b) and WBe_{22} (d) measured in $\mu_0 H = 0$ mT. Vertical dashed lines represent equal-entropy constructions. The horizontal dashed line corresponds to the Sommerfeld coefficient γ_n. The solid line is a fit to $C_e/T \propto e^{-\Delta/T}$ in the superconducting state. Insets of panels (b) and (d) show C_p/T versus T^2, from which the values of γ and β were extracted.

the electronic specific heat, $\Delta C_e/\gamma_n T_c \approx 1.39$ for $MoBe_{22}$ [Fig. 5(b)] and $\Delta C_e/\gamma_n T_c \approx 1.21$ for WBe_{22} [Fig. 5(d)], both of which are comparable with the standard value of the Bardeen-Cooper-Schrieffer (BCS) theory ($\Delta C_e/\gamma_n T_c = 1.44$). In the superconducting state, the specific-heat data are well fit by the $C_e/T \propto e^{-\Delta/k_B T}$ expression deduced from the BCS theory, yielding $2\Delta(0)/k_B T_c = 3.28$ and $2\Delta(0)/k_B T_c = 3.53$ for $MoBe_{22}$ and WBe_{22}, respectively. In both cases, the good agreement between the measured data (symbols) and the BCS fit (lines) provides compelling evidence for an *s*-wave isotropic BCS superconducting gap in the electronic density of states, occurring exactly at the Fermi level. The values of $2\Delta(0)/k_B T_c$ are comparable to the weak-coupling value of 3.52, expected from the BCS theory.

Upon applying a magnetic field, the superconducting transitions of both $MoBe_{22}$ and WBe_{22} are gradually suppressed, as summarized in Figs. 5(a) and 5(c). As shown in Fig. 6, the corresponding values of T_c are given in the $H - T$ phase diagram, shown Fig. 6 in red ($MoBe_{22}$) and blue (WBe_{22}). The fit to the Ginzburg-Landau relation $H_{c2}(T) = H_{c2}(0)\frac{1-(T/T_c)^2}{1+(T/T_c)^2}$ (dashed lines) yields $T_c = 2.7$ K and $T_c = 4.3$ K, as well as $\mu_0 H_{c2}(0) = 48$ mT and $\mu_0 H_{c2}(0) = 58$ mT. Interestingly, the values of $H_{c2}(0)$ are a factor of two larger that those reported previously for $MoBe_{22}$ and WBe_{22} [7]. The discrepant $H_{c2}(0)$ values are most likely related to the different level of impurities [36].

C. *ac* susceptibility under applied pressure

In most solid-state systems, the primary effect of a change in temperature is to modify the *occupation* of the energy levels, while the primary effect of applied pressure is to modify the *energy levels* themselves [37]. Clearly, this makes a pressure study very interesting, as it can provide complementary information to temperature. To characterize the behavior of $MoBe_{22}$ and WBe_{22} under applied pressure, we measured the *ac* response in pressures of up to 2.1 GPa. A small piece of indium, embedded in the pressure cell, served as a pressure gauge. Indeed, since its $T_c(p)$ dependence is well-known, we can determine p (in GPa) from the measured T_c (in K) of indium [38]:

$$T_c(p) = T_c(0) - 0.3812\, p + 0.0122\, p^2. \quad (1)$$

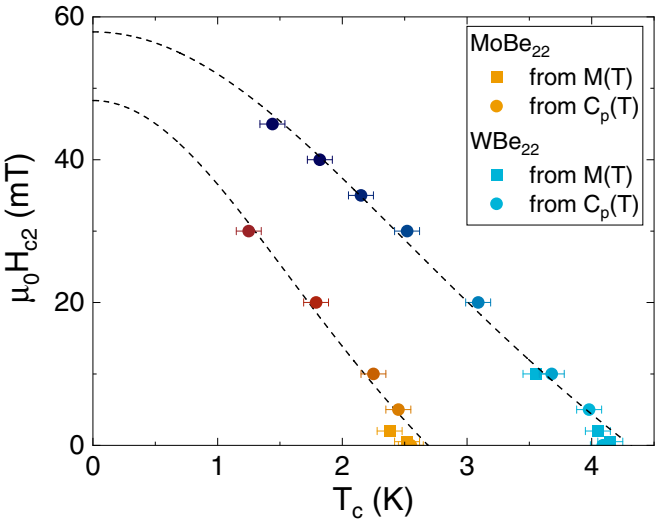

FIG. 6. H–T phase diagram of $MoBe_{22}$ (orange) and WBe_{22} (blue). The values of the critical field $H_{c2}(T)$ are extracted from $M(T)$ (squares) and C_p (circles) data. The dashed lines correspond to a Ginzburg-Landau fit of the data.

Here, $T_c(0) = 3.4$ K, while the coefficients have uncertainties of 0.0002 and 0.0004, respectively. In view of our relatively narrow pressure range (<2.1 GPa) and due to a 30-fold larger linear coefficient compared to the quadratic one, T_c depends almost linearly on p. Even at the highest pressure, the omission of the quadratic term implies an error smaller than 2%. Similar considerations apply to the investigated samples, as confirmed by the linear behavior of T_c versus p, shown in Fig. 7.

To detect the superconducting transition, we use the real part χ' of the *ac* susceptibility (Fig. 7, main panels). Here, T_c is defined as the midpoint of the superconducting transition. In both cases, as the pressure increases from 0 to 2.1 GPa, T_c decreases by *ca.* 0.4 K. The raw *ac* susceptibility data indicate that besides the superconducting transition of In, we also observe a second transition with a lower T_c [see Fig. 7(b)]. Considering its closeness to the T_c of indium and their similar pressure slopes, we attribute the anomaly to a spurious phase of indium (and/or to a mixture of the χ'' and χ' terms of the *ac* response).

TABLE I. Values of the superconducting temperatures T_c and their pressure dependence for $MoBe_{22}$ and WBe_{22}, compared to In (here used as a pressure gauge).

Compound	T_c [K]	dT_c/dp [mK/GPa]	dt/dp [10^{-3} GPa^{-1}]
WBe_{22}	3.975	−192.6	−48.5
$MoBe_{22}$	2.422	−136.2	−56.2
In	3.403	−354.8	−104.3

The T_c values under pressure, as determined from *ac* susceptibility data and shown in the insets of Fig. 7, were fit with a line. The obtained parameters are reported in Table I, with In used as a pressure gauge. Since In is softer than both XBe_{22} compounds, it exhibits a steeper dT_c/dp slope. We note also that, although the absolute slopes of XBe_{22} are rather different [reflecting their different $T_c(0)$ values], the relative slopes, here expressed in terms of the normalized temperature $t = T_c(p)/T_c(0)$, exhibit more regular values. Indeed, in these relative units, one obtains a very similar behavior under pressure for both WBe_{22} and $MoBe_{22}$, as illustrated in the last column of Table I. This result may be justified by the similar Van der Waals and ionic radii of Mo and Be [39].

Recently, the isostructural $ReBe_{22}$ compound was investigated under applied pressures of up to 30 GPa. The value of its T_c was also shown to decrease linearly with pressure [6]. However, despite the similar structure, its relative slope is a factor of 7 lower than that of WBe_{22}. The reason for such a discrepancy is not yet clear, but it might reflect the different atomic radius of Re, compared to those of Mo and W.

Finally, we note that, in general, the linear dependence of T_c on pressure indicates the absence of a pressure-induced structural transition and indirectly confirms the hydrostaticity

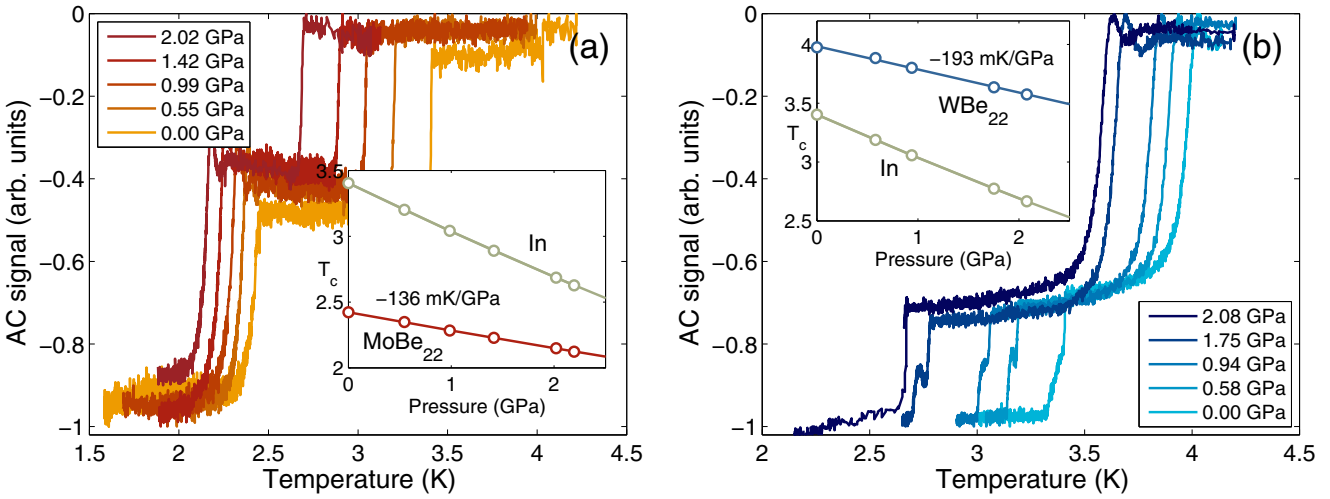

FIG. 7. *ac* susceptibility data versus temperature, measured at various applied pressures for $MoBe_{22}$ (a) and WBe_{22} (b). In both cases, the steep changes in signal reflect the response of the sample and of indium (used here as a pressure gauge). Insets show the almost linear dependence of T_c on pressure. In both cases, error bars are smaller than the symbols.

of the pressure medium. Normally, the critical temperature of a superconductor depends on both the lattice- and electronic properties. Under very general assumptions (weak coupling, BCS superconductors), one can write [see Eq. (2.9) in Ref. [40]:

$$T_c \sim \sqrt{\frac{k}{M}} e^{\frac{-k}{\eta}}, \tag{2}$$

where k is the spring constant (a lattice term), η is a purely electronic term, and M is the atomic mass. Clearly, dT_c/dp depends on the relative magnitude of the pressure-induced changes in lattice versus electronic properties. Under applied pressure, the lattice stiffens, leading to an increase in k. Additionally, η also increases under pressure, although typically much less than k. Since k inside the exponent outweighs k in the prefactor, in general, an increase in k leads to a decrease in T_c. Since in the majority of conventional superconductors the pressure-induced lattice stiffening dominates over the modest changes in electronic properties, this implies a mostly linear decrease of T_c under pressure.

D. Muon-spin rotation study

As a microscopic technique, μSR is very suitable for investigating the nature of pairing symmetry in the superconducting phase. In this case, one applies a moderate- to low-magnetic field, transverse to the muon-spin direction (TF-μSR), and follows the evolution of the muon polarization decay as a function of temperature. Besides the (usually small) depolarization due to the nuclear magnetic moments, below T_c, one observes an increase in the decay rate due to the field modulation from the flux-line lattice (FLL) in the superconducting phase [41]. Such modulation is considerable for fields slightly above H_{c1} and it disappears just below H_{c2}. For optimal results (i.e., to achieve a relatively large decay rate with only a moderate suppression of T_c) one typically applies a field twice H_{c1}, usually above 20 mT. However, in our case, the H_{c2} value of both $MoBe_{22}$ and WBe_{22} is quite low (only about 50 mT, see Fig. 6). This makes it rather difficult to study these compounds *via* TF-μSR, in particular, $MoBe_{22}$, whose T_c and muon depolarization rate are low. Measurements under applied pressure are even more challenging. This is mostly due to the low fraction of signal coming from the sample (typically 2/3 being due to the pressure cell) and the similarity of the relaxation rates of muons stopped in the pressure cell with those stopped in the sample. For these reasons, the remainder of our paper focuses only on WBe_{22}.

To track the additional field-distribution broadening due to the FLL in the mixed superconducting state, the magnetic field was applied in the normal state, prior to cooling the sample below T_c. After the field-cooling protocol, the TF-μSR measurements were performed at various temperatures upon warming. Figure 8(a) shows two representative TF-μSR spectra collected in the superconducting (0.3 K) and the normal state (5 K) in an applied field of 40 mT. Additional TF-μSR spectra collected at 15 mT exhibit similar features (not shown). The inhomogeneous field distribution due to the FLL is reflected in an enhanced depolarization rate below T_c. In this case, the TF-μSR spectra can be modeled by the following

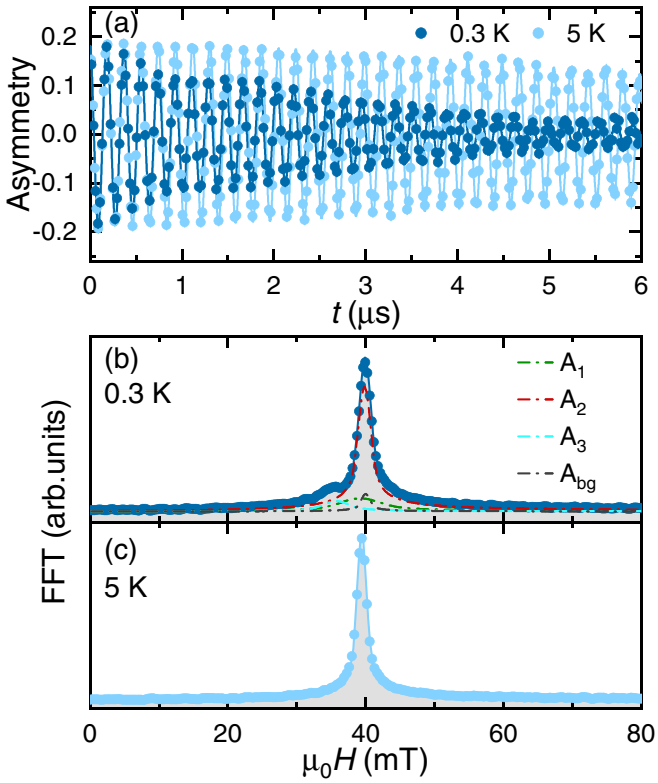

FIG. 8. (a) TF-μSR time-domain spectra of WBe_{22} collected at $T = 0.3$ K and $T = 5$ K in an applied field of 40 mT. The respective Fourier transforms are shown in (b) and (c). Below T_c, three oscillations are needed to reproduce the data. Solid lines are fits to Eq. (8) using three oscillations. Note the absence of a diamagnetic shift below T_c in panel (b)

expression:

$$A_{\rm TF}(t) = \sum_{i=1}^{n} A_i \cos(\gamma_\mu B_i t + \phi) e^{-\sigma_i^2 t^2/2} + A_{\rm bg} \cos(\gamma_\mu B_{\rm bg} t + \phi). \tag{3}$$

Here, A_i and $A_{\rm bg}$ represent the initial muon-spin asymmetries for muons implanted in the sample and sample holder, respectively, with the latter not undergoing any depolarization. B_i and $B_{\rm bg}$ are the local fields sensed by implanted muons in the sample and sample holder, $\gamma_\mu = 2\pi \times 135.53$ MHz/T is the muon gyromagnetic ratio, ϕ is a shared initial phase, and σ_i is a Gaussian relaxation rate of the ith component. The number of required components is material dependent [42]. We find that, similarly to the $ReBe_{22}$ superconductor [5], $n = 3$ is sufficient to describe the TF-μSR spectra of WBe_{22}. The fast-Fourier-transform (FFT) spectra of the TF-μSR datasets at $T = 0.3$ K and $T = 5$ K are shown in Figs. 8(b) and 8(c). The solid lines represent fits to Eq. (3) using three oscillations i.e., $n = 3$) in the superconducting state and one oscillation in the normal state. The derived Gaussian relaxation rates as a function of temperature are summarized in the inset of Fig. 9.

Above T_c, the relaxation rate caused by nuclear magnetic moments is small and temperature independent, but below T_c it starts to increase due to the onset of the FLL and the increase of superfluid density. At the same time, a diamagnetic field

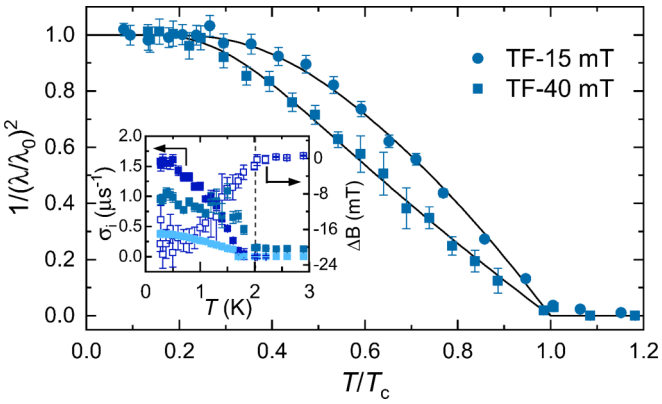

FIG. 9. Superfluid density of WBe_{22} versus temperature, as determined from TF-μSR measurements at $\mu_0 H = 15$ and 40 mT. The inset shows the temperature dependence of the three components of the μSR rate $\sigma_i(T)$ at 40 mT (left axis) and the diamagnetic field shift (right axis). Lines represent fits to a fully gapped s-wave model with a single superconducting gap (see text for details).

shift appears below T_c (see inset of Fig. 9). In the case of multicomponent oscillations, the first-term in Eq. (3) describes the field distribution as the sum of n Gaussian relaxations [42]:

$$P(B) = \gamma_\mu \sum_{i=1}^{n} \frac{A_i}{\sigma_i} \exp\left[-\frac{\gamma_\mu^2 (B - B_i)^2}{2\sigma_i^2}\right]. \quad (4)$$

Then, the first and second moments of the field distribution can be calculated by

$$\langle B \rangle = \sum_{i=1}^{n} \frac{A_i B_i}{A_{\rm tot}} \quad \text{and} \quad (5)$$

$$\langle B^2 \rangle = \frac{\sigma_{\rm eff}^2}{\gamma_\mu^2} = \sum_{i=1}^{n} \frac{A_i}{A_{\rm tot}} \left[\frac{\sigma_i^2}{\gamma_\mu^2} - (B_i - \langle B \rangle)^2\right], \quad (6)$$

where $A_{\rm tot} = \sum_{i=1}^{n} A_i$. The superconducting Gaussian relaxation rate related to the FLL ($\sigma_{\rm sc}$) can be extracted by subtracting the nuclear contribution according to $\sigma_{\rm sc} = \sqrt{\sigma_{\rm eff}^2 - \sigma_{\rm n}^2}$, where $\sigma_{\rm n}$ is the nuclear relaxation rate.

Since $\sigma_{\rm sc}$ is directly related to the magnetic penetration depth (and thus to the superfluid density), the superconducting gap value and its symmetry can be investigated by measuring the temperature-dependent $\sigma_{\rm sc}(T)$. Note that the upper critical field of WBe_{22} is relatively small (58 mT) compared to the fields used in the TF-μSR study (15 and 40 mT). Hence, the effects of the overlapping vortex cores with increasing field should be considered when extracting the magnetic penetration depth λ from $\sigma_{\rm FLL}$. For WBe_{22}, the effective magnetic penetration depth λ was calculated by means of [41,43]

$$\sigma_{\rm FLL} = 0.172 \frac{\gamma_\mu \Phi_0}{2\pi} (1 - h)[1 + 1.21(1 - \sqrt{h})^3] \lambda^{-2}, \quad (7)$$

where $h = H_{\rm appl}/H_{c2}$ and $H_{\rm appl}$ is the applied magnetic field. The calculated inverse-square of the magnetic penetration depth is proportional to the superfluid density $\lambda^{-2}(T) \propto \rho_{\rm sc}(T)$ and is shown in Fig. 9 for WBe_{22}. Below $T_c/3$, the two superfluid densities $\rho_{\rm sc}(T)$, determined *via* TF-15 and TF-40 mT μSR measurements, are practically independent of temperature. This is in agreement with the specific-heat data, shown in Fig. 5, indicating a fully gapped superconducting state. Therefore, we applied an s-wave model to analyze the $\rho_{\rm sc}(T)$ data:

$$\rho_{\rm sc}(T) = 1 + 2 \int_{\Delta(T)}^{\infty} \frac{E}{\sqrt{E^2 - \Delta^2(T)}} \frac{\partial f}{\partial E} dE, \quad (8)$$

Here, $f = (1 + e^{E/k_{\rm B}T})^{-1}$ is the Fermi function, and the temperature dependence of the gap is assumed to follow $\Delta(T) = \Delta_0 \tanh\{1.82[1.018(T_c/T - 1)]^{0.51}\}$ [44,45], where Δ_0 is the gap value at zero temperature (here assumed as the only adjustable parameter). As shown by solid lines in Fig. 9, the temperature-dependent $\lambda^{-2}(T)$ is consistent with an s-wave model with a single gap for both applied fields. For TF-15 mT, the zero-temperature magnetic penetration depth is $\lambda_0 = 168(2)$ nm and the estimated gap value is $\Delta_0 = 1.80(5)\, k_{\rm B} T_c$. The latter is fully compatible with the standard BCS prediction ($\Delta_0 = 1.76\, k_{\rm B} T_c$), confirming the weakly coupled superconductivity. For TF-40 mT, we find $\lambda_0 = 105(3)$ nm and $\Delta_0 = 1.35(5)\, k_{\rm B} T_c$. In this case, due to the low H_{c2}, even an applied field of 40 mT suppresses the superconducting gap significantly.

Finally, although high-pressure μSR measurements did not provide quantitative results, we can still draw qualitative conclusions. The evolution of the μSR relaxation rate as a function of temperature suggests a suppression of T_c with applied pressure. In addition, within the experimental error, we could not detect a change in the nature of superconductivity—the s-wave pairing is preserved up to at least $p = 2.1$ GPa. Finally, the lack of significant changes in relaxation down to the lowest temperature is compatible with the lack of a possible pressure-induced magnetic order.

IV. CONCLUSIONS

By combining results of magnetization, specific-heat, and μSR experiments, we investigated the superconductivity of $MoBe_{22}$ and WBe_{22}. Both systems exhibit a weakly-coupled BCS-like superconducting state below $T_c = 2.7$ K ($MoBe_{22}$) and $T_c = 4.3$ K (WBe_{22}). The modest values of the electronic specific-heat coefficient ($\gamma_n = 6.8$ mJ mol$_{\rm f.u.}^{-1}$ K^{-2} and 10.0 mJ mol$_{\rm f.u.}^{-1}$ K^{-2}), as well as the low upper critical field values [$\mu_0 H_{c2}(0) = 48$ mT and 58 mT] are all compatible with a standard BCS-like behavior. In both cases, high-pressure *ac*-susceptibility and μSR results show a linear decrease of T_c with pressure with a similar slope ($dt/dp \sim -50 \times 10^{-3}$ GPa^{-1}) and no change in the nature of superconducting pairing.

ACKNOWLEDGMENTS

This paper is based on experiments performed at the Swiss Muon Source SμS at the Paul Scherrer Institute, Villigen, Switzerland. We thank R. Khasanov for helpful discussions and assistance. This work was financially supported in part by the Schweizerische Nationalfonds zur Förderung der Wissenschaftlichen Forschung (SNF), Grant No. 200021-169455. T.S. acknowledges the support of the Natural Science Foundation of Shanghai (Grants No. 21ZR1420500 and No. 21JC1402300). E.S. is grateful for the support of the Christiane Nüsslein-Volhard Stiftung.

[1] R. L. Falge Jr., Superconductivity of hexagonal beryllium, Phys. Lett. A **24**, 579 (1967).

[2] D. Duan, Y. Liu, Y. Ma, Z. Shao, B. Liu, and T. Cui, Structure and superconductivity of hydrides at high pressures, Natl. Sci. Rev. **4**, 121 (2017).

[3] D. V. Semenok, A. G. Kvashnin, I. A. Kruglov, and A. R. Oganov, Actinium hydrides AcH_{10}, AcH_{12}, and AcH_{16}, as high-temperature conventional superconductors, J. Phys. Chem. Lett. **9**, 1920 (2018).

[4] E. Bucher and C. Palmy, Superconductivity and isotope effect in $Be_{22}X$ compounds and molybdenum, Phys. Lett. A **24**, 340 (1967).

[5] T. Shang, A. Amon, D. Kasinathan, W. Xie, M. Bobnar, Y. Chen, A. Wang, M. Shi, M. Medarde, H. Q. Yuan, and T. Shiroka, Enhanced T_c and multiband superconductivity in the fully-gapped $ReBe_{22}$ superconductor, New J. Phys. **21**, 073034 (2019).

[6] J. Lim, A. C. Hire, Y. Quan, J. Kim, L. Fanfarillo, S. R. Xie, R. S. Kumar, C. Park, R. J. Hemley, Y. K. Vohra, R. G. Hennig, P. J. Hirschfeld, G. R. Stewart, and J. J. Hamlin, High-pressure study of the low-Z rich superconductor $Be_{22}Re$, Phys. Rev. B **104**, 064505 (2021).

[7] N. N. Matyushenko, A. A. Matsakova, and N. S. Pugachev, Superconductivity of some transition metal-beryllium compounds, Ukr. Fiz. Zh. **18**, 672 (1973).

[8] P. Donze, F. Heiniger, J. Muller, M. Peter, and P. Spitzli, Electronic properties of superconducting compounds with a minor fraction of transition metal atoms, in *Proceedings of the International Conference on Low Temperature Physics*, edited by J. F. Allen, D. M. Finlayson, and D. M. McCall (St. Andrews University Press, St. Andrews, Scotland, 1969), Vol. 2, pp. 1021–1024.

[9] A. Amon, E. Svanidze, R. Cardoso-Gil, M. N. Wilson, H. Rosner, M. Bobnar, W. Schnelle, J. W. Lynn, R. Gumeniuk, C. Hennig, G. M. Luke, H. Borrmann, A. Leithe-Jasper, and Y. Grin, Noncentrosymmetric superconductor BeAu, Phys. Rev. B **97**, 014501 (2018).

[10] A. Amon, A. Ormeci, M. Bobnar, L. G. Akselrud, M. Avdeev, R. Gumeniuk, U. Burkhardt, Y. Prots, C. Hennig, A. Leithe-Jasper, and Y. Grin, Cluster formation in the superconducting complex intermetallic compound $Be_{21}Pt_5$, Acc. Chem. Res. **51**, 214 (2018).

[11] A. Amon, I. Zelenina, P. Simon, M. Bobnar, M. Naumann, E. Svanidze, F. Arnold, H. Borrmann, U. Burkhardt, W. Schnelle, E. Hassinger, A. Leithe-Jasper, and Y. Grin, Tracking aluminium impurities in single crystals of the heavy-fermion superconductor UBe_{13}, Sci. Rep. **8**, 10654 (2018).

[12] A. Amon, E. Svanidze, Y. Prots, M. Nicklas, U. Burkhardt, A. Ormeci, A. Leithe-Jasper, and Y. Grin, $Y_4Be_{33}Pt_{16}$—A non-centrosymmetric cage superconductor with multi-centre bonding in the framework, Dalton Trans. **49**, 9362 (2020).

[13] E. Svanidze, A. Amon, M. Nicklas, Y. Prots, M. Juckel, H. Rosner, U. Burkhardt, M. Avdeev, Y. Grin, and A. Leithe-Jasper, Superconductivity and magnetism in $R_4Be_{33}Pt_{16}$ (R = Y, La–Nd, Sm–Lu): A family of crystallographically complex non-centrosymmetric compounds, Phys. Rev. Materials **5**, 074801 (2021).

[14] P. Koželj, M. Juckel, A. Amon, Y. Prots, A. Ormeci, U. Burkhardt, M. Brando, A. Leithe-Jasper, Y. Grin, and E. Svanidze, Non-centrosymmetric superconductor $Th_4Be_{33}Pt_{16}$ and heavy-fermion $U_4Be_{33}Pt_{16}$ cage compounds, Sci. Rep. **11**, 22352 (2021).

[15] A. Amon, Rare earth and actinide beryllides: Structural chemistry and physical properties, in *Handbook on the Physics and Chemistry of Rare Earths: Including Actinides*, edited by J.-C. G. Bünzli and V. K. Pecharsky (Elsevier, Amsterdam, 2021), Vol. 59, Chap. 319, pp. 93–140.

[16] J. Beare, M. Nugent, M. N. Wilson, Y. Cai, T. J. S. Munsie, A. Amon, A. Leithe-Jasper, Z. Gong, S. L. Guo, Z. Guguchia, Y. Grin, Y. J. Uemura, E. Svanidze, and G. M. Luke, μSR and magnetometry study of the type-I superconductor BeAu, Phys. Rev. B **99**, 134510 (2019).

[17] R. Khasanov, R. Gupta, D. Das, A. Amon, A. Leithe-Jasper, and E. Svanidze, Multiple-gap response of type-I noncentrosymmetric BeAu superconductor, Phys. Rev. Res. **2**, 023142 (2020).

[18] R. Khasanov, R. Gupta, D. Das, A. Leithe-Jasper, and E. Svanidze, Single-gap versus two-gap scenario: Specific heat and thermodynamic critical field of the noncentrosymmetric superconductor BeAu, Phys. Rev. B **102**, 014514 (2020).

[19] A. Leithe-Jasper, H. Borrmann, and W. Hönle, *Laboratory of High Safety Standard (LHS)*, Scientific Report (Max Planck Institute for Chemical Physics of Solids, Dresden, 2006).

[20] H. Okamoto and L. E. Tanner, The Be-W (Beryllium-Tungsten) system, Bull. Alloy Phase Diagrams **7**, 356 (1986).

[21] Binary Alloy Phase Diagrams, edited by T. B. Massalski, H. Okamoto, P. R. Subramanian, and L. Kacprzak, (ASM International, Materials Park, OH, 1990).

[22] P. I. Kripyakevich and E. I. Gladyshevskii, The crystal structures of beryllium-rich compounds in the systems Mo-Be and W-Be, Soviet Phys.-Cryst. **8**, 349 (1963) [Kristallografiya **8**, 449 (1963)].

[23] R. M. Paine and J. A. Carrabine, Some new intermetallic compounds of beryllium, Acta Crystallogr. **13**, 680 (1960).

[24] See Supplemental Material at http://link.aps.org/supplemental/10.1103/PhysRevMaterials.6.064804 for crystallographic information for the $MoBe_{22}$ and WBe_{22} phases.

[25] A. Suter and B. M. Wojek, Musrfit: A free platform-independent framework for μSR data analysis, Phys. Procedia **30**, 69 (2012).

[26] S. Klotz, *Techniques in High Pressure Neutron Scattering* (CRC Press, Boca Raton, FL, 2013).

[27] M. S. Torikachvili, S. K. Kim, E. Colombier, S. L. Bud'ko, and P. C. Canfield, Solidification and loss of hydrostaticity in liquid media used for pressure measurements, Rev. Sci. Instrum. **86**, 123904 (2015).

[28] Z. Shermadini, Iron based pnictide and chalcogenide superconductors studied by muon spin spectroscopy, Ph.D. thesis, TU Dresden, Dresden, 2014.

[29] R. Khasanov, Z. Guguchia, A. Maisuradze, D. Andreica, M. Elender, A. Raselli, Z. Shermadini, T. Goko, F. Knecht, E. Morenzoni, and A. Amato, High pressure research using muons at the Paul Scherrer Institute, High Press. Res. **36**, 140 (2016).

[30] M. Bendele, A. Amato, K. Conder, M. Elender, H. Keller, H.-H. Klauss, H. Luetkens, E. Pomjakushina, A. Raselli, and R. Khasanov, Pressure Induced Static Magnetic Order in Superconducting $FeSe_{1-x}$, Phys. Rev. Lett. **104**, 087003 (2010).

[31] S. Samson, The crystal structure of the intermetallic compound $Mg_3Cr_2Al_{18}$, Acta Crystallogr. **11**, 851 (1958).

[32] S. Samson, The crystal structure of the intermetallic compound $ZrZn_{22}$, Acta Crystallogr. **14**, 1229 (1961).

[33] P. Kripyakevich and O. Zarechnyuk, RCr_2Al_{20} compounds in systems of rare earth metals and calcium, and their crystal structures, Dopov. Akad. Nauk Ukr. RSR, Ser. A **30**, 364 (1968).

[34] F. Laves and H. Witte, Investigations in the Mg-Cu-Al System, Especially on the $MgCu_2$-$MgAl_2$ Section, Metallwirtschaft **15**, 15 (1936).

[35] Due to difficulties in cutting the samples into a suitable shape and in estimating the exact W/$MoBe_{22}$ sample fraction, the exact demagnetization factor could not be taken into account. Given the nearly spherical sample shape, if a value of $N_d = 1/3$ is taken into account, the resultant χ is reduced very slightly. On the other hand, EDX analyses estimate that the samples contain 40% of the Mo/WBe_{22} phase (see Sec. II), resulting in a significant reduction of the χ value. Nonetheless, the bulk nature of superconductivity in Mo/WBe_{22} samples is confirmed *via* specific-heat measurements (see Sec. III).

[36] Y. N. Ovchinnikov and V. Z. Kresin, Critical magnetic field in layered superconductors, Phys. Rev. B **52**, 3075 (1995).

[37] H. Drickamer, The effect of high pressure on the electronic structure of solids, in *Solid State Physics*, edited by F. Seitz and D. Turnbull (Academic Press, New York, 1965), Vol. 17, pp. 1–133.

[38] A. Eiling and J. S. Schilling, Pressure and temperature dependence of electrical resistivity of Pb and Sn from 1–300 K and 0–10 GPa—use as continuous resistive pressure monitor accurate over wide temperature range; superconductivity under pressure in Pb, Sn, and In, J. Phys. F: Met. Phys. **11**, 623 (1981).

[39] Atomic and ionic radii, http://abulafia.mt.ic.ac.uk/shannon/radius.php, accessed Jan. 10, 2022.

[40] J. J. Hamlin, Superconductivity studies at extreme pressure, Ph.D. thesis, Washington University, St. Louis, Missouri, 2007.

[41] E. H. Brandt, Properties of the ideal Ginzburg-Landau vortex lattice, Phys. Rev. B **68**, 054506 (2003).

[42] A. Maisuradze, R. Khasanov, A. Shengelaya, and H. Keller, Comparison of different methods for analyzing μSR line shapes in the vortex state of type-II superconductors, J. Phys.: Condens. Matter **21**, 075701 (2009), and references therein.

[43] W. Barford and J. M. F. Gunn, The theory of the measurement of the London penetration depth in uniaxial type II superconductors by muon spin rotation, Physica C: Superconductivity **156**, 515 (1988).

[44] M. Tinkham, *Introduction to Superconductivity*, 2nd ed. (Dover Publications, Mineola, NY, 1996).

[45] A. Carrington and F. Manzano, Magnetic penetration depth of MgB_2, Physica C: Superconductivity **385**, 205 (2003).